



Using magnetic dynamics to measure the spin gap in a candidate Kitaev material



Xinyi Jiang^{1,9}, Qingzheng Qiu^{1,9}, Cheng Peng^{1,2,9}, Hoyoung Jang^{1,3,4}, Wenjie Chen¹, Xianghong Jin¹, Li Yue¹, Byungjune Lee^{1,5}, Sang-Youn Park^{1,3}, Minseok Kim³, Hyeong-Do Kim^{1,3}, Xinqiang Cai¹, Qizhi Li¹, Tao Dong¹, Nanlin Wang^{1,6}, Joshua J. Turner^{2,7}, Yuan Li^{1,6}, Yao Wang^{1,6} ✉ & Yingying Peng^{1,6} ✉

Spin-orbit entangled materials have attracted widespread interest due to the novel magnetic phenomena arising from the interplay between spin-orbit coupling and electronic correlations. However, the intricate nature of spin interactions within Kitaev materials complicates the precise measurement of low-energy spin excitations. Using $\text{Na}_2\text{Co}_2\text{TeO}_6$ as an example, we study these low-energy spin excitations using the time-resolved resonant elastic x-ray scattering (tr-REXS). Our observations unveil remarkably slow spin dynamics at the magnetic peak, whose recovery timescale is several nanoseconds. This timescale aligns with the extrapolated spin gap of $\sim 1 \mu\text{eV}$, obtained by density matrix renormalization group (DMRG) simulations in the thermodynamic limit. The consistency demonstrates the efficacy of tr-REXS in discerning low-energy spin gaps inaccessible to conventional spectroscopic techniques.

Spin-orbit entangled insulators, shaped by the intricate interplay between electron correlation and spin-orbit coupling, exhibit a range of exotic phases, including axion insulators, topological Mott insulators, and Kitaev materials^{1–3}. Kitaev materials, in particular, have drawn significant attention due to their honeycomb magnetic lattice geometry, which offers a theoretically exact solution under idealized conditions^{4,5}. In this model, bond-dependent anisotropic Kitaev interactions between adjacent spins lead to magnetic frustration and significant quantum fluctuations⁶. In reality, spin-orbit entangled Kitaev candidate materials often exhibit complicated magnetic interactions, such as the Heisenberg interaction and off-diagonal spin exchange, aside from the Kitaev interactions^{6–8}. Consequently, most candidate materials exhibit magnetic order at low temperatures instead of a quantum spin liquid (QSL) ground state^{8–11}. Nevertheless, these ordered phases offer crucial insights, as their symmetry and magnetic excitations shed light on the underlying interactions. This information is essential for evaluating and potentially tuning these systems toward a QSL state, thus advancing the understanding of spin-orbit entangled quantum materials^{5,12}.

Several transition-metal materials, including $\alpha\text{-RuCl}_3$ ^{11,13} and $\text{H}_3\text{LiIr}_2\text{O}_6$ ⁸, have been proposed as candidates for realizing the Kitaev model. Apart from these, $\text{Na}_2\text{Co}_2\text{TeO}_6$ is distinguished as a promising

candidate due to its more compact $3d$ orbitals which exhibit stronger spin couplings compared to the weakly localized $5d$ - and $4d$ -electron systems⁶. The spin-orbital coupling (SOC) within $3d$ orbitals of each Co atom gives rise to an effective spin-1/2 configuration on the honeycomb lattice. The complicated spin interactions and fluctuations within the spin-orbit entangled $\text{Na}_2\text{Co}_2\text{TeO}_6$ leads to frustration and quantum fluctuations, yielding a diverse magnetic phase diagram^{14–16}. At low temperatures, the system transitions from a paramagnetic state to a two-dimensional (2D) antiferromagnetic ordered state at 31 K, followed by the emergence of a 3D ordered state below 26.7 K^{15–19}. Neutron scattering studies reveal that the low-energy spin excitations are diffusing below the 2D order transition temperature of 31 K, which have impeded the precise determination of its spin gap¹⁶.

Characterizing small spin gaps is significant for identifying phases in quantum materials. Historical examples include the debates over whether various spin systems exhibit a gapped or gapless spin liquid, such as the initial variational calculations proposing a gapless Dirac quantum spin liquid (QSL) state in the spin-1/2 Heisenberg model on kagome lattices²⁰, while DMRG studies suggested a gapped QSL state with distinct properties²¹. Beyond spin liquids, the presence of spin gap signals non-trivial

¹International Center for Quantum Materials, School of Physics, Peking University, Beijing, China. ²Stanford Institute for Materials and Energy Science, Stanford University and SLAC National Accelerator Laboratory, Menlo Park, CA, USA. ³PAL-XFEL, Pohang Accelerator Laboratory, POSTECH, Pohang, Gyeongbuk, Republic of Korea. ⁴Photon Science Center, POSTECH, Pohang, Gyeongbuk, Republic of Korea. ⁵Max Planck POSTECH/Korea Research Initiative, Center for Complex Phase Materials, Pohang, Gyeongbuk, Republic of Korea. ⁶Collaborative Innovation Center of Quantum Matter, Beijing, China. ⁷Linac Coherent Light Source, SLAC National Accelerator Laboratory, Menlo Park, CA, USA. ⁸Department of Chemistry, Emory University, Atlanta, GA, USA. ⁹These authors contributed equally: Xinyi Jiang, Qingzheng Qiu, Cheng Peng. ✉e-mail: yao.wang@emory.edu; yingying.peng@pku.edu.cn

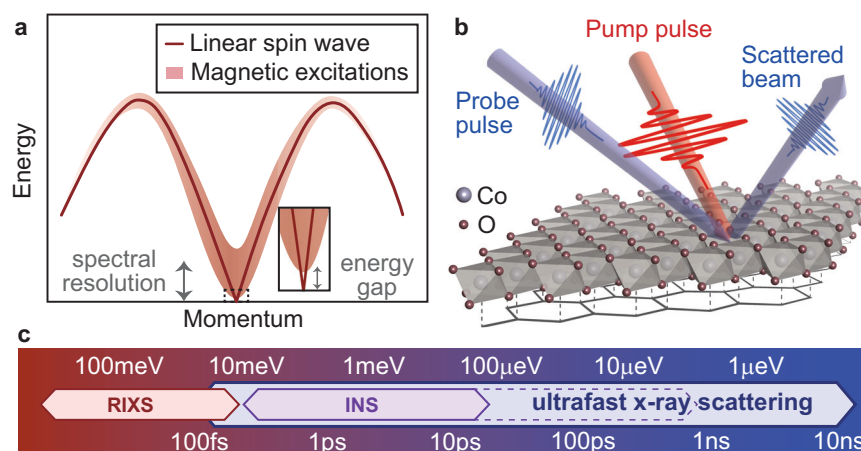


Fig. 1 | Ultrafast characterization of low-energy spin gaps. **a** Illustration of gapless spin-wave excitations (solid line) and the continuum in frustrated magnets. A closer look at the low-energy region is provided in the inset. The arrows sketch the spectral resolution and the small spin gap. **b** Experimental setup for the trREXS, showing the optical pump (red) and x-ray probe (blue). The honeycomb lattice under the crystal structure indicates the lattice formed by the Co atoms, significant in the Kitaev

model. **c** Comparison of energy resolutions of scattering spectra and their corresponding timescales. The red arrow sketches the range of energy resolutions accessible through RIXS; the purple arrow indicates the energy resolution commonly achieved by INS, with the dashed line representing resolutions that require additional effort. Ultrafast trREXS measurement can cover a broad energy resolution range based on the observed timescales.

topological properties and thermal transport properties in low-dimensional materials^{22–26}. The ability to directly detect the spin gap is crucial to resolving these questions. Thus, various conventional experimental techniques have been employed to characterize the spin gap, as shown in Fig. 1a, including specific heat²⁷, thermal conductivity^{28,29}, electron spin resonance (ESR)^{9,30}, nuclear magnetic resonance (NMR)³¹, inelastic neutron scattering (INS)³², and resonant inelastic x-ray scattering (RIXS)³³. However, detecting spin gaps smaller than microelectron volts by these traditional techniques remains a significant challenge, limited by the lower bounds of measured energy and temperature, as well as energy resolution.

An alternative method for probing small-energy excitations has been proposed in the time domain. As shown in Fig. 1c, the characteristic time is inverse to a dominant energy scale. Thus, a small spin gap, which is beyond the resolution of RIXS or INS measurements, reflects a relatively long timescale that can be discerned using pump-probe techniques. For example, time-resolved optical spectroscopy has successfully disentangled low-energy bosonic excitations through their distinct timescales³⁴; time-resolved x-ray scattering spectroscopy has revealed a collective charge fluctuation with characteristic energy in the sub-meV range³⁵; x-ray photon correlation spectroscopy has been utilized to reveal sub-meV antiferromagnetic domain fluctuations³⁶. In this scenario, ultrafast x-ray scattering emerges as a promising avenue to achieve microelectron volt energy resolution for a specific magnetic excitation by analyzing the corresponding finite-momentum dynamics in the time domain. By monitoring dynamics exceeding longer than several nanoseconds, one can access an energy resolution of sub- μeV scales, which is crucial for probing small spin gaps.

To this end, we employ time-resolved resonant elastic x-ray scattering (Tr-REXS) to reveal long-term magnetic dynamics at picoseconds to nanoseconds timescales in the Kitaev candidate material $\text{Na}_2\text{Co}_2\text{TeO}_6$, as sketched in Fig. 1b. With the high-momentum resolution and time-resolved capabilities, we are able to directly investigate the fluence- and temperature-dependence of magnetic dynamics after pump. By a DMRG simulation of its model Hamiltonian, we further show that observed slow recovery dynamics reflects the small spin gaps in these types of magnetic materials. Thus, we establish this methodology by determining a spin gap of $\sim 0.6 \mu\text{eV}$ in $\text{Na}_2\text{Co}_2\text{TeO}_6$.

Results

Spectral characterization in equilibrium

The $\text{Na}_2\text{Co}_2\text{TeO}_6$ crystal is characterized by a hexagonal space group $P6_322$. Its magnetic moments are predominantly contributed by the valence

electron in the high-spin electronic configuration ($t_{2g}^5 e_g^2$) of Co^{2+} ions, with both spin and orbital angular momenta contributing to the magnetic moment³⁷. Each edge-sharing CoO_6 octahedra can be effectively regarded as a spin-1/2 state, forming a two-dimensional (2D) honeycomb lattice, as depicted in Fig. 1b. The energy-momentum-resolved REXS spectrum exhibits a pronounced peak at $\mathbf{q} = (-0.5, 0, 0.62)$ at 30 K, as shown in Fig. 2a, consistent with previous study^{16,38}. Its intensity maximizes at two incident x-ray energies of 778.9 eV and 777.3 eV. The multi-peak resonances are related to the different electronic states, and the spectral features of the x-ray absorption spectrum of $\text{Na}_2\text{Co}_2\text{TeO}_6$ are similar to the CoO reference spectrum, confirming the Co^{2+} state³⁹ [see Supplementary Note 1]. As the temperature decreases below 2D magnetic phase transition temperature $T_{2D} \sim 31$ K, both peaks exhibit a coincided rise of intensity [see Supplementary Note 1 for details], reflecting their associations with the magnetic order^{16,17}. Both scattering peaks remain finite while largely suppressed above 31 K, indicating a subleading structural order that coexists with magnetic instability. Analyzing the temperature dependency of these two scattering peaks facilitates the differentiation between magnetic and structural contributions. The scattering intensity at 778.9 eV displays a strong temperature dependence immediately below 31 K, indicating a predominant magnetic contribution; conversely, the intensity at 777.3 eV remains evident above 31 K and climbs more gradually below 31 K, implying larger structural contribution. Our XRD studies demonstrate that this superstructure peak is almost independent of temperature below 31 K [see Supplementary Note 2], allowing us to subtract it to isolate the pure magnetic signal. Our time-resolved experiment results show that the suppression of the superstructure peak is very small ($\sim 2\%$, within the noise level) [see Supplementary Note 2].

Light-induced dynamics of the magnetic scattering peak

By driving $\text{Na}_2\text{Co}_2\text{TeO}_6$ out of equilibrium using a laser pulse, we analyze the subsequent changes in the magnetic structure using Tr-REXS. We exploit the two resonant scattering peaks (highlighted in Fig. 2) near $\mathbf{q} = (-0.5, 0, 0.62)$ to quantify the magnetic excitations. The energy gap of $\text{Na}_2\text{Co}_2\text{TeO}_6$ is determined as ~ 2 eV by the optical absorption spectrum (inset of Fig. 3a). The small absorption peak at ~ 1 eV arises from the d-d transition of octahedral Co^{2+} ⁴⁰. To decipher the dynamics of this magnetic order and the related magnetic excitations, we use both the below-gap 800 nm (~ 1.55 eV) pump laser and above-gap 400 nm (~ 3.1 eV) pump laser to excite the resonant magnetic peaks.

As shown in Fig. 3a, the evolution of the 778.9 eV REXS peak intensity, induced by an 800 nm pump laser, exhibits a prolonged dynamics at 23 K,

Fig. 2 | Equilibrium characterization of magnetic order. **a** REXS spectra for $\text{Na}_2\text{Co}_2\text{TeO}_6$ at 30 K, showing the scattering intensity distribution around $H = -0.5$ r.l.u. (lower) and the integrated intensity for wavevectors between $H = -0.502$ and -0.498 r.l.u. (upper). The two shaded peaks in the upper panel highlight the two dominant resonant energies (777.3 eV and 778.9 eV) associated with the magnetic order. **b** Temperature dependence of the scattering signals at the two different incident energies. The intensities are fitted using an empirical equation and revealed the 2D magnetic transition temperature $T_{2D} = 31$ K.

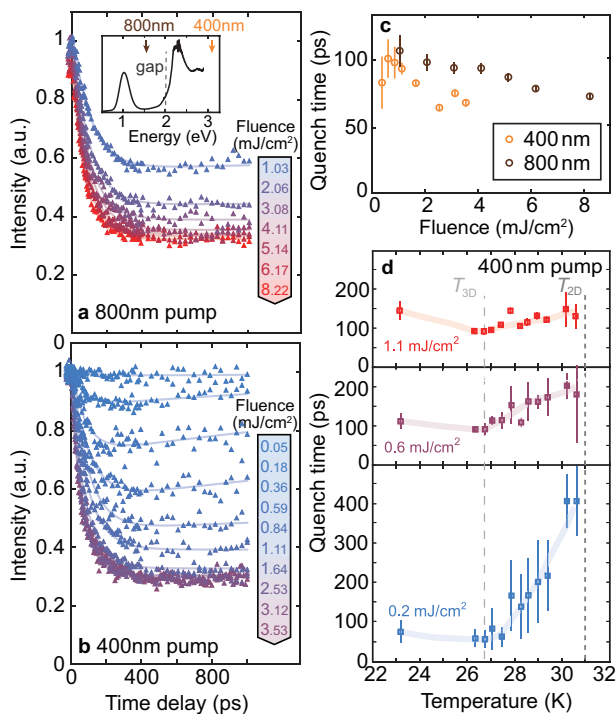
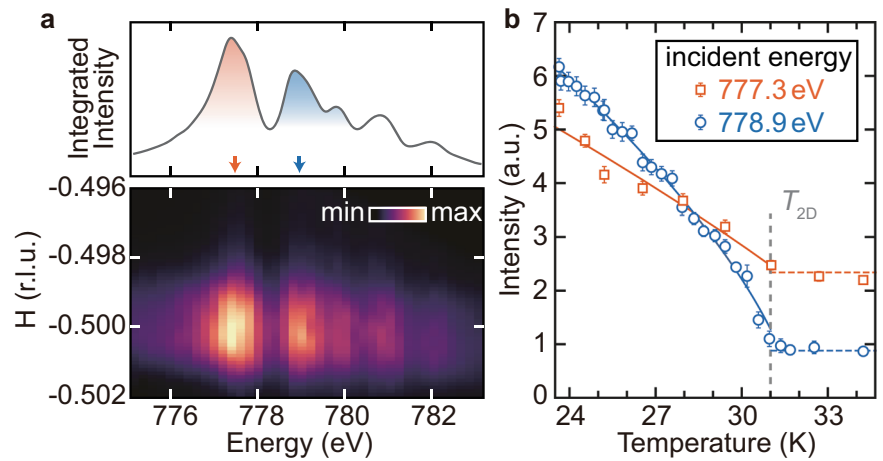


Fig. 3 | Evolution of the magnetic scattering peak. **a, b** Evolution of the magnetic scattering intensity for the 778.9 eV resonance induced by **(a)** 800 nm and **(b)** 400 nm pumps with various fluences, normalized by the equilibrium spectral intensities. The solid curves delineate the double-exponential fitting using Eq. (1). The pump-probe measurements are conducted at 23 K. The inset shows the optical absorption spectra of $\text{Na}_2\text{Co}_2\text{TeO}_6$, with arrows highlighting the 400 nm and 800 nm photon energies, respectively. The dashed line indicates the band gap of ~ 2 eV. **c** The quench time τ_q extracted from **(a, b)** as a function of pump fluence. **d** Temperature dependence of the quench times for a 400 nm pump with different pump fluences. The dashed lines denote the transition temperatures of the 3D and 2D magnetic orders.

manifesting as a gradual decay after pump (denoted as “quenching”) and a subsequent slow recovery back to equilibrium. This behavior can be described by a double-exponential function [see fitting details in Supplementary Note 3]:

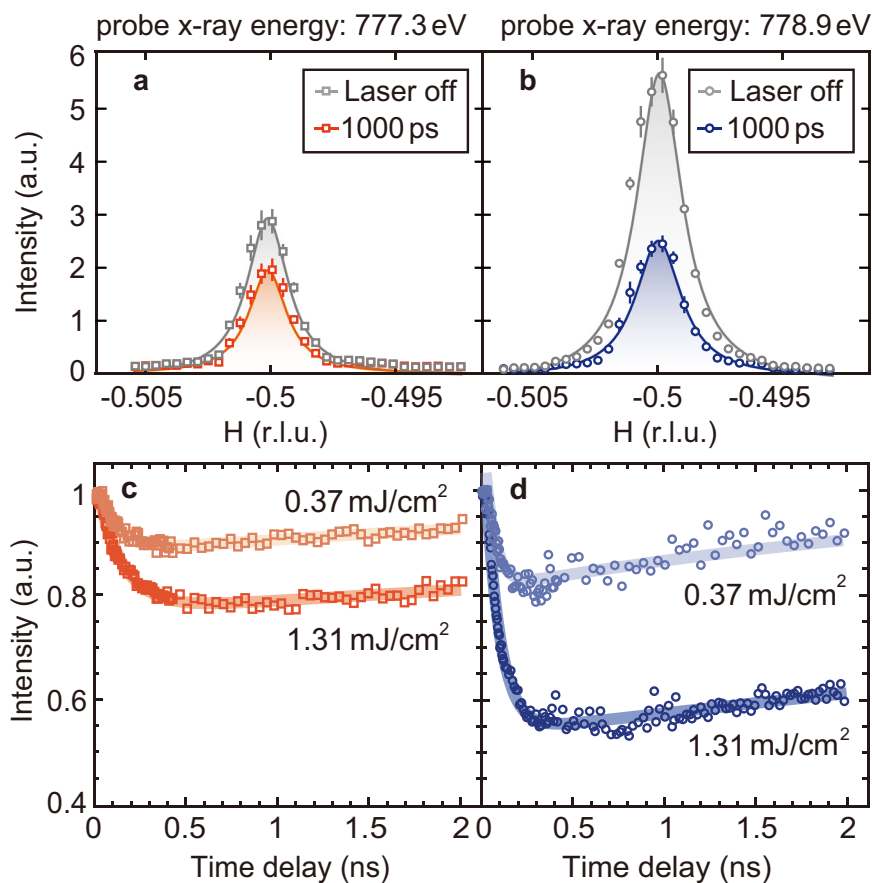
$$I(\Delta t) = I_{\text{res}} + I_{\text{quench}} \left[e^{-\Delta t/\tau_q} + (1 - e^{-\Delta t/\tau_r}) \right]. \quad (1)$$

Here, I_{quench} is the intensity portion affected by the pump laser and depends on the pump fluence, while I_{res} represents the residual intensity. To highlight the relative changes, these intensities are normalized by the equilibrium scattering peak intensity. The two prolonged dynamical processes are characterized by the characteristic quenching time τ_q and recovery time τ_r , respectively. Similar slow dynamics also appear in the evolution induced by an above-gap 400 nm pump (see Fig. 3b). This similarity suggests that the dynamics induced by these long-term dynamics can be regarded as the evolution of spin excitations. The dynamics induced by the below-gap 800 nm pump is less likely due to two-photon absorption since two-photon absorption requires more fluence (at least an order of magnitude higher than the above-gap pump⁴¹) to induce a similar suppression of the magnetic intensity. Due to the optical resonance, the absorption rate is much higher in 400 nm, resulting in a more pronounced response and higher fidelity when fitting the characteristic times [see Supplementary Note 4]. Specifically, the I_{quench} saturates at a fluence of 2.5 mJ/cm² and 5 mJ/cm² for the 400 nm and 800 nm pumps, respectively. For convenience of analyzing the magnetic excitation timescales and their fluence dependence, we primarily focus on the 400 nm pump in this work.

The light-induced demagnetization in $\text{Na}_2\text{Co}_2\text{TeO}_6$ occurs within a timescale of 50 to 100 ps, as characterized by τ_q (see Fig. 3c). This demagnetization process slightly accelerates with an increase in pump fluence, attributed to photocarrier screening effects^{42,43}. Notably, the order parameter decays significantly slower than in CDW materials^{44–48} and Mott insulators^{49–53}. This phenomenon can be presumably attributed to the localized spins in cobalts, which hinder direct coupling between the electronic orbital degree of freedom and the spins. Without this direct coupling, the demagnetization is primarily driven by the strong phonon-magnon coupling in $\text{Na}_2\text{Co}_2\text{TeO}_6$ as also evidenced by thermal conductivity^{29,54}. This mechanism aligns with observations in other materials like InMnAs ⁵⁵ and MnBi_2Te_4 ⁵⁶, where localized spin moments and significant spin-lattice coupling are present. Similar to the REXS peak at 778.9 eV, the dynamics of the 777.3 eV resonant peak exhibit a slow demagnetization process with comparable timescales [see Supplementary Note 5]. Due to the mixture of magnetic and structural contributions, the I_{quench} is smaller for the 777.3 eV REXS peak.

Aside from the similarity with the dynamics induced by the below-gap 800 nm laser, relation between the prolonged dynamics induced by the 400 nm laser and spin excitations is further confirmed through the temperature dependence. As shown in Fig. 3d, the quenching time τ_q exhibits a significant increase as the temperature approaches $T_{2D} = 31$ K from below. This trend reflects the strong magnetic fluctuations near the phase transition^{51,57–59}, which has been also observed in other Kitaev materials such as $\alpha\text{-RuCl}_3$ ⁵¹. A minor difference from $\alpha\text{-RuCl}_3$ is the disruption of the monotonic trend below 26.7 K in $\text{Na}_2\text{Co}_2\text{TeO}_6$, where another 3D magnetic order starts to develop. This observation suggests an interplay between two

Fig. 4 | Destruction and recovery of magnetic diffraction with a 400 nm excitation. **a, b** The variation of the (−0.5, 0, 0.62) magnetic peak before and after pump excitation (1000 ps, 400 nm) with 777.3 eV and 778.9 eV at 23 K. The superstructure peaks are subtracted from the data. The grey shade indicates the change in intensity caused by photo-excitation. Solid lines are fit using a Lorentzian function. Error bars represent Poisson counting error. **c, d** Magnetic intensity normalized by laser-off data as a function of time delay with 777.3 eV (**c**) and 778.9 eV (**d**) at 23 K. The blue and red lines display the results of fitting, corresponding to pump fluence of 0.37 and 1.31 mJ/cm² respectively.



distinct magnetic orders in Na₂Co₂TeO₆, a phenomenon that warrants further investigation but is beyond the scope of this work.

Unlike the quench time which reflects the transition to excited states, the recovery process back to equilibrium characterizes the low-energy magnetic excitations. Therefore, we examine the long-time evolution of the two Tr-REXS peaks following the 400 nm pump. A comparison between the spectral shapes for both resonant peaks at equilibrium and 1000 ps indicates that the peak width remains essentially consistent, distinct from the broadening observed in thermal fluctuations⁶⁰ (see Fig. 4a, b). We use the Lorentzian function to fit the half-width at half-maximum (HWHM) of the magnetic peak. The correlation length of the magnetic order $\xi = 1/\text{HWHM}$, where HWHM is expressed in units of a^* ($a^* = 2\pi/(\sqrt{3}/2 \times a_0)$). The magnetic correlation length is $\sim 130 a_0$ and 700 \AA , which is not limited by experimental resolution [see Supplementary Note 6]. Furthermore, the superstructure modulations have a negligible effect on the measured magnetic correlation length [see Supplementary Note 2]. Figure 4c and d present the corresponding fluence dependence of the magnetic dynamics for the two x-ray energies. For a relatively strong pump of 1.31 mJ/cm², the long-term recovery can be characterized as $\tau_r = 8.66 \pm 0.47 \text{ ns}$ for the 777.3 eV and $11.43 \pm 0.38 \text{ ns}$ for the 778.9 eV peak. Reducing the pump fluence leads to a decrease in τ_r , contradicting again to the heat diffusion process [see Supplementary Note 7]. At a fluence of 0.37 mJ/cm², we observe a saturation in the recovery timescale for the 778.9 eV peak [see Supplementary Note 7], yielding a $\tau_r = 2.54 \pm 0.14 \text{ ns}$. This timescale coincides with the results for the 777.3 eV peak at the same fluence ($\tau_r = 3.94 \pm 0.17 \text{ ns}$). Their proximity further underlines their association with the material's intrinsic low-energy states, independent of pump and probe conditions. The phenomenon of prolonged relaxation is not unique to Na₂Co₂TeO₆, but is also observed in other materials with intricate magnetic phases, such as another Kitaev candidate $\alpha\text{-RuCl}_3$ ⁴² and multiferroic TbMnO₃. These nanosecond-long relaxations are believed to occur due to nearly degenerate magnetic ground and excited states, influenced by frustrated interactions^{15–19}. Therefore, the

timescale of recovery quantitatively encodes information about these low-energy states.

Spin gap measurement from the Heisenberg-Kitaev model

To elucidate the slow recovery dynamics in Na₂Co₂TeO₆ and its relation to the low-energy spin structure, we simulate the spin-1/2 Kitaev-Heisenberg Hamiltonian to describe the microscopic states of Na₂Co₂TeO₆^{61,62}. This model captures the superexchange between each Co atom in a hexagonal structure, as illustrated in Fig. 5a. The cobalt atoms in an octahedral crystal field assume a high-spin ($t_{2g}^5 e_g^2$) configuration in their 3d orbitals. Without trigonal splitting, an effective orbital momentum $L_{\text{eff}} = 1$ with spin-orbit coupling splits the three-fold degenerate t_{2g} orbitals into $j_{\text{eff}} = 1/2, 3/2$, and $5/2$ states, with $j_{\text{eff}} = 1/2$ as the ground state. The superexchange interactions between nearest-neighbor Co atoms, via $t_{2g}\text{-}t_{2g}$, $t_{2g}\text{-}e_g$, and $e_g\text{-}e_g$ channels, are mediated by the 2p orbitals of intervening oxygen atoms in a 90° of Co–O–Co bond geometry [see Fig. 5b]. This configuration leads to a coupling between the spins at two Co sites (denoted as i and j) perpendicular to the exchange path, i.e. $S_i^\alpha S_j^\gamma$ ($\gamma = x, y, z$ depends on the hexagon plane orientation). Deviations from perfect octahedral geometry introduce off-diagonal spin interactions, resulting in the Kitaev-Heisenberg Hamiltonian:

$$\begin{aligned} \mathcal{H} = & \sum_{\langle i,j \rangle} J_1 \mathbf{S}_i \cdot \mathbf{S}_j + \sum_{\langle\langle i,j \rangle\rangle} J_2 \mathbf{S}_i \cdot \mathbf{S}_j + \sum_{\langle\langle\langle i,j \rangle\rangle\rangle} J_3 \mathbf{S}_i \cdot \mathbf{S}_j \\ & + \sum_{\langle i,j \rangle} K S_i^\alpha S_j^\gamma + \sum_{\langle i,j \rangle} \Gamma \left(S_i^\alpha S_j^\beta + S_i^\beta S_j^\alpha \right) \\ & + \sum_{\langle i,j \rangle} \Gamma' \left(S_i^\alpha S_j^\gamma + S_i^\gamma S_j^\alpha + S_i^\beta S_j^\delta + S_i^\delta S_j^\beta \right). \end{aligned} \quad (2)$$

Here, the Heisenberg interactions are described by the first, second, and third nearest-neighbor spin-exchange J_1, J_2 , and J_3 ; K is the bond-dependent Kitaev interactions, with $\{\alpha, \beta, \gamma\}$ denoting the three types of anisotropic terms for the three nearest-neighbor directions. The symmetric off-diagonal

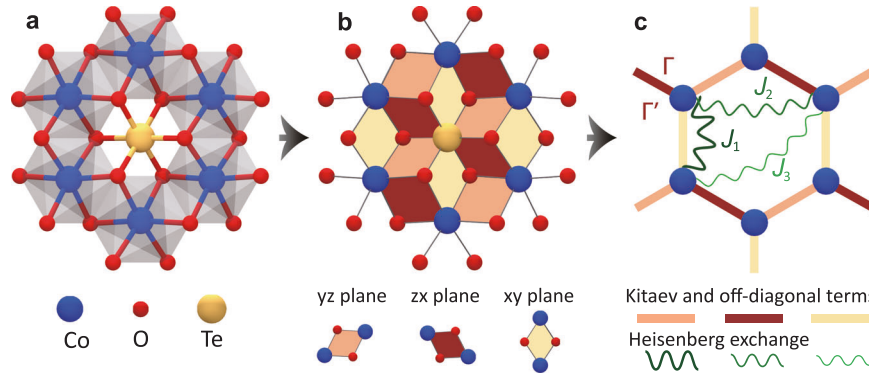


Fig. 5 | Lattice structure of Na₂Co₂TeO₆ and the microscopic model schematics on the honeycomb layer. **a** Co-Te-O layer with Co (blue) atoms forming the honeycomb structure. Each nearest-neighbor Co pair is connected through two oxygen (red), and the Te (yellow) is placed at the center of each hexagon. The edge-sharing octahedra are represented by the gray cage surrounding each Co. **b** The pseudospin superexchange of Co mediated by O gives rise to the anisotropic spin

terms K , and the octahedra distortion results in the symmetric off-diagonal terms $\{\Gamma, \Gamma'\}$. The rotations of $\{\alpha, \beta, \gamma\}$ are represented by $\{y, z, x\}$ (orange), $\{z, x, y\}$ (red) and $\{x, y, z\}$ (yellow), respectively. **c** The isotropic Heisenberg interaction between the nearest neighbor, next nearest neighbor, and third nearest neighbor for Co are shown as $\{J_1, J_2, J_3\}$, the orientations of Kitaev and off-diagonal spin interactions are shown as the orange, red, and yellow bonds.

terms, Γ and Γ' , appear in the Hamiltonian due to the octahedra distortion mentioned above. We follow the spectral fitting in ref.⁶¹ and choose the coupling coefficients as $J_1 = -0.1$ meV, $J_2 = 0.3$ meV, $J_3 = 0.9$ meV, $K = -9$ meV, $\Gamma = 1.8$ meV, and $\Gamma' = 0.3$ meV [see Supplementary Note 8 for the discussions of other model parameters].

Employing the DMRG method⁶³, renowned for its accuracy in analyzing strongly correlated systems, we simulate the electronic structure of Na₂Co₂TeO₆, with a specific focus on the spin excitation gap. For relatively small systems, DMRG enables direct calculation of the first several excited states, thereby identifying the spin excitation gap defined as the energy difference between the ground state and the first excited state. The deduced gap values for a 4×4 and 6×4 clusters are $\Delta = 54.6 \mu\text{eV}$ and $32.4 \mu\text{eV}$, respectively. (These unit cells are oriented along the e_1 and e_2 vectors, as shown in the inset of Fig. 6b). Notably, the gap decreases as the system size increases, indicating a finite-size effect and necessitating extrapolation to the thermodynamic limit.

Despite the impracticality of a direct finite-size scaling for excited states due to computational demands, we employ an indirect extrapolation to determine the spin gap. Systems larger than 18×4 exhibit a spatial distribution of the ground-state spin-spin correlation function $F^z(r)$ that decay exponentially along the horizontal direction. A correlation length ξ can be extracted from fitting the correlation function (see the Methods). Accounting for relativistic effects near a quantum phase transition, we employ the $\Delta \propto 1/\xi$ relationship to infer the spin gap⁶⁴. Specifically, we simulate the $F^z(r)$ for systems with various L_x where ξ can be reliably determined. The inverse of these ξ -values displays strong linearity with $1/L_x$, as shown in Fig. 6a. Extrapolating this size dependency to the thermodynamic limit ($1/L_x \rightarrow 0$), we obtain an intersection of $1/\xi \sim 0.02a_0^{-1}$, with a_0 representing the lattice constant. This agrees with the experimental magnetic correlation length within the error bar. By comparing the fitted linearity with the energy gaps calculated for smaller systems, we establish a correlation between Δ and $1/\xi$ (velocity of excitations), yielding

$\xi\Delta/a_0 = 63.9 \pm 4.5 \mu\text{eV}$. Therefore, our DMRG simulation of the Kitaev-Heisenberg gives a spin gap $\Delta \sim 1.3 \mu\text{eV}$ in the thermodynamic limit. Our calculations have also considered other sets of parameters reported by INS studies [see Supplementary Note 8]. These models develop potentially gapless modes, which are inconsistent with the INS experimental data and our measured magnetic dynamics indicating the presence of a gap.

The long-term recovery timescale is predominantly governed by the low-energy states and can be approximated by the Rabi oscillation period across the spin gap. Therefore, the characteristic time derived from our simulation yields $\tau_r = h/\Delta \sim 3.2$ ns, as shown in Fig. 6b. This simulated

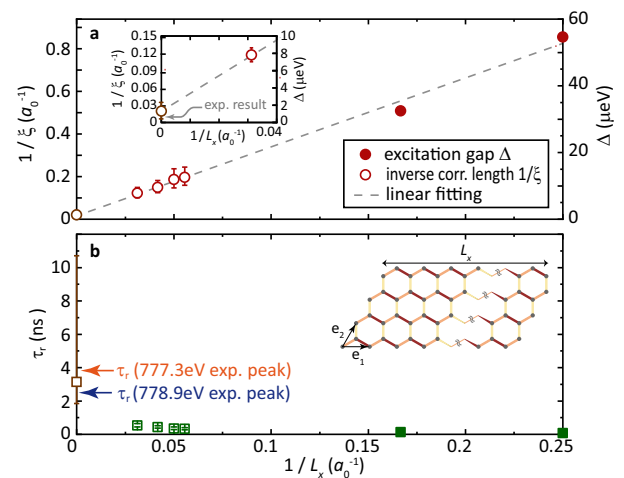


Fig. 6 | Simulation of energy and timescales using the Kitaev-Heisenberg model. **a** The excitation gap Δ (closed circles) and inverse correlation length $1/\xi$ (open circles) simulated using the Kitaev-Heisenberg model for $L_x \times 4$ -systems with different sizes. The dashed line denotes the linear fitting for the Δ and $1/\xi$, with the thermodynamic-limit extrapolation (intersection) represented by the gray open circle. The inset contrasts the simulated and experimental correlation lengths near the thermodynamic limit. The value of $1/\xi$ has an error bar of 0.014. **b** Characteristic timescales τ_r (green squares) extracted from the Rabi oscillation across the excitation gap. The gray square marks the thermodynamic-limit extrapolation. The two arrows highlight experimentally determined τ_r using two x-ray energies. The inset shows the quasi-1D geometry, with bond colors indicating the Kitaev superexchanges in Fig. 5.

timescale is consistent with the experimentally observed τ_r at low frequencies for both x-ray peaks (3.94 ns and 2.54 ns).

Discussion

The consistency between the spin gap determined through DMRG simulations and the characteristic recovery time identified in trREXS experiments reflects the viability of measuring ultra-small energy gaps using pump-probe x-ray experiments. Importantly, such determinations are also feasible with experimentally measured correlations, indicating the correlation-gap relation. A supporting evidence is that the experimentally measured correlation length ($\xi = 130a_0$) translates into an energy gap $\Delta \sim 0.6 \mu\text{eV}$, using the $\xi\Delta/a_0$ obtained in Fig. 6a, yielding a characteristic time of 6.4 ns. This timescale falls within the range of the recovery times (τ_r) observed for the strong and weak pump conditions. The extracted

correlation length from 2D order can be connected to the spin gap as the spin gap is dispersionless along the L direction in $\text{Na}_2\text{Co}_2\text{TeO}_6$ [see Supplementary Note 6]. INS experiments on $\text{Na}_2\text{Co}_2\text{TeO}_6$ reveal a spin gap of ~ 1 meV, which is determined as the energy at the maximum intensity^{15,16,65}. However, the spin excitation has a bandwidth, and its weak spectral weight extends down to the elastic line. Such a small spin gap below 1 μeV will be buried by the large elastic peak in INS studies. Therefore, our results do not contradict the INS studies, which provide an upper boundary for the spin gap. Our results are consistent with a recent μSR experiment which has revealed prevalent spin dynamics down to 3.3 K^{14} , suggesting significant quantum fluctuations and allowing the existence of a spin gap much smaller than 1 meV. Notably, excitation continua below spin-wave excitations have been observed in ordered magnets. For example, a recent INS study on the magnetically ordered $\text{Na}_2\text{BaCo}(\text{PO}_3)_2$ revealed a spin excitation continuum induced by strong quantum fluctuations below the spin-wave modes⁶⁶. Similarly, in the Kitaev material $\alpha\text{-RuCl}_3$, which develops magnetic order at low temperatures, neutron scattering studies revealed a broad continuum beneath the sharp magnon excitations. This continuum is interpreted as evidence of fractionalized excitations arising from Kitaev-type interactions^{10,12}. While our study utilizes $\text{Na}_2\text{Co}_2\text{TeO}_6$ as an example, due to the significance of its spin gap, this methodology is broadly applicable to diverse systems where the gap size ranges from 0.1 to 100 μeV . Such gap sizes correspond to picosecond to nanosecond timescales, which can be effectively revealed by the recovery dynamics.

While the correlation length and associated timescale exhibit consistent orders of magnitude, it is important to emphasize that the Hubbard-Kitaev model, as a single-orbital spin model, simplifies the material by focusing on the key ingredients. It does not account for charge transfer between different atoms, the presence of 3D magnetic order, or spin-phonon couplings. As a result, the model does not capture the demagnetization process observed in the initial 100 ps of the dynamics. The DMRG simulation is designed to examine the recovery process, governed by the low-energy states. Moreover, experimental results are subject to fitting inaccuracies and the intrinsic noise prevalent in long-duration measurements. As such, when comparing simulation outcomes with experimental data, one should consider potential error cancellations and focus on the order of magnitude, avoiding over-interpretation.

Our findings contribute to the ongoing exploration of spin gaps in complex magnetic systems. Our time-resolved REXS study reveals a small spin gap hidden in the diffuse spin excitation, which is challenging to measure by neutron scattering. This novel discovery highlights the advantages of trREXS in identifying spin gaps compared to other techniques. For instance, neutron backscattering and neutron spin-echo measurements also offer the energy resolutions of μeV , but require a large amount of single crystals. In contrast, our method requires only a small amount, thus extending its applicability to a wider range of samples. While transport techniques such as NMR and AC susceptibility can cover hundreds of nanoseconds to much longer, their energy range is much lower than trREXS⁶⁷. The demonstration of time-resolved x-ray scattering spectroscopy in detecting small spin gaps with its unique merits and unprecedented precision opens innovative pathways for the detailed study and engineering of quantum magnets.

Methods

Sample preparation

The high-quality single crystals of $\text{Na}_2\text{Co}_2\text{TeO}_6$ used in this study were grown with a flux method³⁷. The hexagonal-shaped crystal flake used in this study had the dimensions of $\sim 3\text{ mm} \times 3\text{ mm} \times 0.2\text{ mm}$ (lattice parameters: $a = b = 5.25\text{ \AA}$, $c = 11.19\text{ \AA}$). The sample was cleaved and examined by x-ray diffraction measurements (XRD) before experiments to confirm its excellent quality. Single crystal x-ray diffraction measurements were performed using the custom-designed x-ray instrument equipped with a Xenocs Genix3D Mo $K\alpha$ (17.48 keV) x-ray source, which provides $\sim 2.5 \times 10^7$

photons/sec in a beam spot size of $150\text{ }\mu\text{m}$ at sample position⁶⁸. We also performed the x-ray reciprocal space mapping measurements. The sample was mounted on a Huber 4-circle diffractometer. During data collection, the sample was continuously rotated at a rate of $0.005^\circ/\text{s}$. The 3-dimensional (3D) mapping of momentum space was realized by taking images in 0.1° sample-rotation increments. We fitted the lattice parameters with a hexagonal lattice for the single crystal and indexed the Bragg peaks. Then we can transform the data into HKL reciprocal space. Supplementary Fig S3 shows the diffuse scattering mapping of the $Q = (H, 0.5, L)$ plane.

Optical measurements

The optical transmission data were collected at room temperature and converted to the absorption spectra. For the photon energy range from 0.5 to 2.7 eV, the measurement was performed on a Bruker 80V Fourier transform infrared spectrometer. For the photon energy range from 1.3 to 4 eV, the measurement was carried out on a home-built transmission measurement setup with a deuterium-halogen light source (Ideaoptics iDH2000-BSC) and a highly sensitive spectrometer (Ideaoptics Nova). Then, the transmission spectra from the two measurements were combined by normalizing the data in the overlapped range.

tr-RSXS measurements

The tr-RSXS experiments were carried out at the SSS-RSXS endstation of PAL-XFEL⁶⁹. The sample was mounted on a six-axis open-circle cryostat manipulator with a base temperature of $\sim 20\text{ K}$. The sample surface was perpendicular to the crystalline c axis, and the horizontal scattering plane was parallel to the bc plane. X-ray pulses with ~ 80 fs pulse duration and 60 Hz repetition rate were used for the soft x-ray probe. The x-ray was linear horizontal polarized (π -polarization), and the photon energy was tuned to Co L_3 edge ($\sim 778\text{ eV}$). Since the 2D magnetic order is L -independent, we fixed the scattering angle of detector at $2\theta = 156^\circ$, which provides $L = 0.62$ r.l.u. at $H = -0.5$ r.l.u. The temperature dependence of the scattering signals was fitted by an empirical function $I(T) = a\{1 - [(T + b)/(1 + b)]^c\}$ as shown in Fig. 2b⁷⁰. The equilibrium sample temperature had been calibrated following the magnetic transition temperature reported in ref.¹⁶.

We utilized a Ti:sapphire laser to provide optical lasers at 1.55 eV (800 nm) and 3.1 eV (400 nm) with a pulse duration of ~ 50 fs and a repetition rate of 30 Hz. The 800 nm is converted to 400 nm through BBO crystal. Both σ -polarized (perpendicular to the scattering plane) and π -polarized (parallel to the scattering plane) laser pulses were used to excite $\text{Na}_2\text{Co}_2\text{TeO}_6$, showing similar transient responses, indicating no laser polarization dependence. To simplify our experimental setup, we chose an 800 nm laser with σ -polarization and a 400 nm laser with π -polarization, considering that the polarization direction of the laser pulse underwent a 90-degree rotation after frequency doubling. The overall time resolution was ~ 108 fs, determined by measuring the pump-probe cross-correlation. The optical laser was nearly parallel to the incident X-ray beam, with an angle difference of less than 1° . The pump fluence ranged from 0.1 to $8\text{ mJ}/\text{cm}^2$. The x-ray spot size at the sample position was $\sim 100(H) \times 200(V)\text{ }\mu\text{m}^2$ (FWHM), while the optical laser spot diameter was about $\sim 500\text{ }\mu\text{m}$ (FWHM). The X-ray repetition rate was twice that of the pump pulses, enabling the comparison of diffraction signals before and after pump excitation.

Extrapolation of the excitation gap

To estimate the gap in the thermodynamic limit, we simulated the first excited-state energy for the Heisenberg-Kitaev model on a four-leg ladder using excited-state method of DMRG developed on ITensor Software Library⁷¹. However, due to the significantly increased computing costs after extending the cylinder's length L_x , our excited-state simulations were restricted to $L_x = 4$ and 6 (in units of a_0). In simulations of larger systems, we switched to an indirect simulation of the gap using ground-state properties obtained from DMRG⁷². Specifically, we estimated the ground-state spin-spin correlation length using a code based on a high-

performance matrix product state algorithm library GraceQ/MPS2⁷³. The number of DMRG block states was constrained owing to the absence of spin-rotational symmetry. We maintained multiple bond dimensions of the matrix product state representation of the ground state at each sweep, with a maximum bond dimension of 2048, and a typical truncation error of $\epsilon \approx 10^{-7}$. The results presented in the main text had been extrapolated to $\epsilon = 0$ to minimize the cutoff error. Note that the cylinder geometry, chosen as $L_x \times L_y$ cluster with the open boundary condition along the \mathbf{e}_1 direction and periodic boundary condition along the \mathbf{e}_2 direction, destroyed the continuous spin symmetry in the system so that the spin correlation function $F^\alpha(r) = \langle S_{x_0}^\alpha S_{x_0+r}^\alpha \rangle - \langle S_{x_0}^\alpha \rangle \langle S_{x_0+r}^\alpha \rangle$ for $\alpha = x$ and y decayed exponentially, but $F^z(r)$ saturated to a constant while the spin gap was finite. We obtained the spin correlation length by fitting the correlation function $F^z(r)$ through $e^{-r/\xi}$. The extrapolation into the thermodynamic limit yields a $\xi = 49a_0$.

The correlation length was extrapolated to the thermodynamic limit $L_x \rightarrow \infty$, using the linear function $1/\xi = \alpha(1/L_x) + \beta$. This fitting function faithfully described the scaling behavior, reaching the fitted intercept $\beta = 0.02059 \pm 0.01348$. Here, the ξ was expressed in the unit of unit cell along the \mathbf{e}_1 direction, depicted as a_0 . As the linear relation between $1/\xi$ and $1/L_x$ had been verified, we reversely extrapolated the linear function backward to the short L_x region where the energy difference between the ground state and the first excited state was evaluated through the excited-state method of DMRG. Then we used the least-square approach to determine the $\xi\Delta/a_0$ constant by minimizing the energy error against the two simulated excitation gaps for small clusters. The fitting result showed $\xi\Delta/a_0 = 63.9 \pm 4.5 \mu\text{eV}$, where the small residual error indicated the validity of this linear fitting. Alternatively, if we picked only one out of the 4×4 - or 6×4 -cluster to fit the constant, the estimation of $\xi\Delta/a_0$ would be $66.4 \mu\text{eV}$ or $58.4 \mu\text{eV}$, respectively. This estimated error was consistent with the fitting residual calculated above.

Data availability

All data needed to evaluate the conclusions in the paper are present in the paper and/or the Supplementary Materials. Additional data related to this paper may be requested from the authors.

Received: 19 April 2024; Accepted: 20 January 2025;

Published online: 01 February 2025

References

- Witczak-Krempa, W., Chen, G., Kim, Y. B. & Balents, L. Correlated quantum phenomena in the strong spin-orbit regime. *Annu. Rev. Condens. Matter Phys.* **5**, 57–82 (2014).
- Banerjee, S., Zhu, W. & Lin, S.-Z. Electromagnetic signatures of a chiral quantum spin liquid. *npj Quantum Mater.* **8**, 63 (2023).
- Wulferding, D. et al. Collective magnetic Higgs excitation in a pyrochlore ruthenate. *npj Quantum Mater.* **8**, 40 (2023).
- Kitaev, A. Anyons in an exactly solved model and beyond. *Ann. Phys.* **321**, 2–111 (2006).
- Takagi, H., Takayama, T., Jackeli, G., Khaliullin, G. & Nagler, S. E. Concept and realization of Kitaev quantum spin liquids. *Nat. Rev. Phys.* **1**, 264–280 (2019).
- Liu, H., Chaloupka, J. & Khaliullin, G. Kitaev spin liquid in 3d transition metal compounds. *Phys. Rev. Lett.* **125**, 047201 (2020).
- Liu, H. & Khaliullin, G. Pseudospin exchange interactions in d^7 cobalt compounds: possible realization of the Kitaev model. *Phys. Rev. B* **97**, 014407 (2018).
- Kitagawa, K. et al. A spin-orbital-entangled quantum liquid on a honeycomb lattice. *Nature* **554**, 341–345 (2018).
- Lin, G. et al. Field-induced quantum spin disordered state in spin-1/2 honeycomb magnet $\text{Na}_2\text{Co}_2\text{TeO}_6$. *Nat. Commun.* **12**, 5559 (2021).
- Do, S.-H. et al. Majorana fermions in the Kitaev quantum spin system $\alpha\text{-RuCl}_3$. *Nat. Phys.* **13**, 1079–1084 (2017).
- Zheng, J. et al. Gapless spin excitations in the field-induced quantum spin liquid phase of $\alpha\text{-RuCl}_3$. *Phys. Rev. Lett.* **119**, 227208 (2017).
- Banerjee, A. et al. Neutron scattering in the proximate quantum spin liquid $\alpha\text{-RuCl}_3$. *Science* **356**, 1055–1059 (2017).
- Han, J.-H. et al. Weak-coupling to strong-coupling quantum criticality crossover in a Kitaev quantum spin liquid $\alpha\text{-RuCl}_3$. *npj Quantum Mater.* **8**, 33 (2023).
- Miao, P. et al. Persistent spin dynamics in magnetically ordered honeycomb-lattice cobalt oxides. *Phys. Rev. B* **109**, 134431 (2024).
- Yao, W., Iida, K., Kamazawa, K. & Li, Y. Excitations in the ordered and paramagnetic states of honeycomb magnet $\text{Na}_2\text{Co}_2\text{TeO}_6$. *Phys. Rev. Lett.* **129**, 147202 (2022).
- Chen, W. et al. Spin-orbit phase behavior of $\text{Na}_2\text{Co}_2\text{TeO}_6$ at low temperatures. *Phys. Rev. B* **103**, L180404 (2021).
- Lee, C. H. et al. Multistage development of anisotropic magnetic correlations in the Co-based honeycomb lattice $\text{Na}_2\text{Co}_2\text{TeO}_6$. *Phys. Rev. B* **103**, 214447 (2021).
- Lefrançois, E. et al. Magnetic properties of the honeycomb oxide $\text{Na}_2\text{Co}_2\text{TeO}_6$. *Phys. Rev. B* **94**, 214416 (2016).
- Bera, A., Yusuf, S., Kumar, A. & Ritter, C. Zigzag antiferromagnetic ground state with anisotropic correlation lengths in the quasi-two-dimensional honeycomb lattice compound $\text{Na}_2\text{Co}_2\text{TeO}_6$. *Phys. Rev. B* **95**, 094424 (2017).
- Ran, Y., Hermele, M., Lee, P. A. & Wen, X.-G. Projected-wave-function study of the spin-1/2 Heisenberg model on the Kagome lattice. *Phys. Rev. Lett.* **98**, 117205 (2007).
- Yan, S., Huse, D. A. & White, S. R. Spin-liquid ground state of the $S = 1/2$ Kagome Heisenberg antiferromagnet. *Science* **332**, 1173–1176 (2011).
- Zhu, F. et al. Topological magnon insulators in two-dimensional van der Waals ferromagnets CrSiTe_3 and CrGeTe_3 : Toward intrinsic gap-tunability. *Sci. Adv.* **7**, eabi7532 (2021).
- Chen, L. et al. Topological spin excitations in honeycomb ferromagnet CrI_3 . *Phys. Rev. X* **8**, 041028 (2018).
- Vu, D. D. et al. Magnon gap mediated lattice thermal conductivity in MnBi_2Te_4 . *Phys. Rev. B* **108**, 144402 (2023).
- Gillig, M. et al. Phononic-magnetic dichotomy of the thermal hall effect in the Kitaev material $\text{Na}_2\text{Co}_2\text{TeO}_6$. *Phys. Rev. Res.* **5**, 043110 (2023).
- Mangeolle, L., Balents, L. & Savary, L. Phonon thermal hall conductivity from scattering with collective fluctuations. *Phys. Rev. X* **12**, 041031 (2022).
- Maple, M. B. et al. Partially gapped Fermi surface in the heavy-electron superconductor URu_2Si_2 . *Phys. Rev. Lett.* **56**, 185–188 (1986).
- Yamashita, M. et al. Thermal-transport measurements in a quantum spin-liquid state of the frustrated triangular magnet $\kappa\text{-(BEDT-TTF)}_2\text{Cu}_2(\text{CN})_3$. *Nat. Phys.* **5**, 44–47 (2009).
- Hong, X. et al. Phonon thermal transport shaped by strong spin-phonon scattering in a Kitaev material $\text{Na}_2\text{Co}_2\text{TeO}_6$. *npj Quantum Mater.* **9**, 18 (2024).
- Björn, M. et al. Gapped magnetic ground state in quantum spin liquid candidate $\kappa\text{-(BEDT-TTF)}_2\text{Cu}_2(\text{CN})_3$. *Science* **372**, 276–279 (2021).
- Mingxuan, F., Takashi, I., Tian-Heng, H. & Young, S. L. Evidence for a gapped spin-liquid ground state in a Kagome Heisenberg antiferromagnet. *Science* **350**, 655–658 (2015).
- Calder, S., Pajerowski, D. M., Stone, M. B. & May, A. F. Spin-gap and two-dimensional magnetic excitations in Sr_2IrO_4 . *Phys. Rev. B* **98**, 220402 (2018).
- Kim, J. et al. Large spin-wave energy gap in the bilayer iridate $\text{Sr}_3\text{Ir}_2\text{O}_7$: Evidence for enhanced dipolar interactions near the Mott metal-insulator transition. *Phys. Rev. Lett.* **109**, 157402 (2012).
- Conte, S. D. et al. Disentangling the electronic and phononic glue in a high- T_C superconductor. *Science* **335**, 1600–1603 (2012).

35. Matteo, M. et al. Ultrafast time-resolved x-ray scattering reveals diffusive charge order dynamics in $\text{La}_{2-x}\text{Ba}_x\text{CuO}_4$. *Sci. Adv.* **5**, eaax3346 (2019).
36. Shpyrko, O. et al. Direct measurement of antiferromagnetic domain fluctuations. *Nature* **447**, 68–71 (2007).
37. Yao, W. & Li, Y. Ferrimagnetism and anisotropic phase tunability by magnetic fields in $\text{Na}_2\text{Co}_2\text{TeO}_6$. *Phys. Rev. B* **101**, 085120 (2020).
38. Yao, W. et al. Magnetic ground state of the Kitaev $\text{Na}_2\text{Co}_2\text{TeO}_6$ spin liquid candidate. *Phys. Rev. Res.* **5**, L022045 (2023).
39. Istomin, S. Y. et al. An unusual high-spin ground state of Co^{3+} in octahedral coordination in brownmillerite-type cobalt oxide. *Dalton Trans.* **44**, 10708–10713 (2015).
40. Barreda-Argüeso, J. A. et al. Crystal-field theory validity through local (and bulk) compressibilities in CoF_2 and KCoF_3 . *J. Phys. Chem. C* **120**, 18788–18793 (2016).
41. Soumah, L., Bossini, D., Anane, A. & Bonetti, S. Optical frequency up-conversion of the ferromagnetic resonance in an ultrathin garnet mediated by magnetoelastic coupling. *Phys. Rev. Lett.* **127**, 077203 (2021).
42. Wagner, J. et al. Nonequilibrium dynamics of $\alpha\text{-RuCl}_3$ - a time-resolved magneto-optical spectroscopy study. *Faraday Discuss.* **237**, 237–258 (2022).
43. Okazaki, K. et al. Photo-induced semimetallic states realised in electron-hole coupled insulators. *Nat. Commun.* **9**, 4322 (2018).
44. Schmitt, F. et al. Transient electronic structure and melting of a charge density wave in TbTe_3 . *Science* **321**, 1649–1652 (2008).
45. Gedik, N. et al. Abrupt transition in quasiparticle dynamics at optimal doping in a cuprate superconductor system. *Phys. Rev. Lett.* **95**, 117005 (2005).
46. Zong, A. et al. Dynamical slowing-down in an ultrafast photoinduced phase transition. *Phys. Rev. Lett.* **123**, 097601 (2019).
47. Zong, A. et al. Ultrafast manipulation of mirror domain walls in a charge density wave. *Sci. Adv.* **4**, eaau5501 (2018).
48. Zong, A. et al. Evidence for topological defects in a photoinduced phase transition. *Nat. Phys.* **15**, 27–31 (2019).
49. Ehrke, H. et al. Photoinduced melting of antiferromagnetic order in $\text{La}_{0.5}\text{Sr}_{1.5}\text{MnO}_4$ measured using ultrafast resonant soft x-ray diffraction. *Phys. Rev. Lett.* **106**, 217401 (2011).
50. Bothschafter, E. M. et al. Dynamic pathway of the photoinduced phase transition of TbMnO_3 . *Phys. Rev. B* **96**, 184414 (2017).
51. Versteeg, R. B. et al. Nonequilibrium quasistationary spin disordered state in $\alpha\text{-RuCl}_3$. *Phys. Rev. B* **105**, 224428 (2022).
52. Dean, M. P. et al. Ultrafast energy- and momentum-resolved dynamics of magnetic correlations in the photo-doped Mott insulator Sr_2IrO_4 . *Nat. Mater.* **15**, 601–605 (2016).
53. Mazzone, D. G. et al. Laser-induced transient magnons in $\text{Sr}_3\text{Ir}_2\text{O}_7$ throughout the Brillouin zone. *Proc. Natl. Acad. Sci.* **118**, e2103696118 (2021).
54. Hong, X. et al. Strongly scattered phonon heat transport of the candidate Kitaev material $\text{Na}_2\text{Co}_2\text{TeO}_6$. *Phys. Rev. B* **104**, 144426 (2021).
55. Wang, J. et al. Ultrafast quenching of ferromagnetism in InMnAs induced by intense laser irradiation. *Phys. Rev. Lett.* **95**, 167401 (2005).
56. Padmanabhan, H., Stoica, V. A. & Kim, P. K. Large exchange coupling between localized spins and topological bands in MnBi_2Te_4 . *Adv. Mater.* **34**, 2202841 (2022).
57. Afanasiev, D. et al. Ultrafast spin dynamics in photodoped spin-orbit Mott insulator Sr_2IrO_4 . *Phys. Rev. X* **9**, 021020 (2019).
58. Zhang, J. et al. Discovery of slow magnetic fluctuations and critical slowing down in the pseudogap phase of $\text{YBa}_2\text{Cu}_3\text{O}_y$. *Sci. Adv.* **4**, eaao5235 (2018).
59. Lovinger, D. J. et al. Influence of spin and orbital fluctuations on Mott-Hubbard exciton dynamics in LaVO_3 thin films. *Phys. Rev. B* **102**, 115143 (2020).
60. Lee, W. et al. Phase fluctuations and the absence of topological defects in a photo-excited charge-ordered nickelate. *Nat. Commun.* **3**, 838 (2012).
61. Songvilay, M. et al. Kitaev interactions in the Co honeycomb antiferromagnets $\text{Na}_3\text{Co}_2\text{SbO}_6$ and $\text{Na}_2\text{Co}_2\text{TeO}_6$. *Phys. Rev. B* **102**, 224429 (2020).
62. Winter, S. M. Magnetic couplings in edge-sharing high-spin d^7 compounds. *J. Phys. Mater.* **5**, 045003 (2022).
63. White, S. R. Density matrix formulation for quantum renormalization groups. *Phys. Rev. Lett.* **69**, 2863–2866 (1992).
64. Eberharter, A. A., Vanderstraeten, L., Verstraete, F. & Läuchli, A. M. Extracting the speed of light from matrix product states. *Phys. Rev. Lett.* **131**, 226502 (2023).
65. Krüger, W. G. F., Chen, W., Jin, X., Li, Y. & Janssen, L. Triple-q order in $\text{Na}_2\text{Co}_2\text{TeO}_6$ from proximity to hidden-SU(2)-symmetric point. *Phys. Rev. Lett.* **131**, 146702 (2023).
66. Sheng, J. et al. Continuum of spin excitations in an ordered magnet. *Innovation* **6**, 100769 (2025).
67. Topping, C. & Blundell, S. Ac susceptibility as a probe of low-frequency magnetic dynamics. *J. Phys.-condens. Mat.* **31**, 013001 (2018).
68. Xiao, Q. et al. Coexistence of multiple stacking charge density waves in kagome superconductor CsV_3Sb_5 . *Phys. Rev. Res.* **5**, L012032 (2023).
69. Jang, H. et al. Time-resolved resonant elastic soft x-ray scattering at Pohang Accelerator Laboratory X-ray Free Electron Laser. *Rev. Sci. Instrum.* **91**, 083904 (2020).
70. Joe, Y. et al. Emergence of charge density wave domain walls above the superconducting dome in 1T-TiSe_2 . *Nat. Phys.* **10**, 421–425 (2014).
71. Fishman, M., White, S. R. & Stoudenmire, E. M. The ITensor Software Library for Tensor Network Calculations. *Sci. Post Phys. Codebases*, 4 (2022).
72. Peng, C., Jiang, Y.-F., Devereaux, T. P. & Jiang, H.-C. Precursor of pair-density wave in doping Kitaev spin liquid on the honeycomb lattice. *npj Quantum Mater.* **6**, 64 (2021).
73. GraceQuantum.org. GraceQ/MPS2: A high-performance matrix product state algorithms library based on GraceQ/tensor. *GitHub* (2021).

Acknowledgements

We acknowledge the valuable discussion with Hong-Chen Jiang, Shaozhi Li, Donna N. Sheng, Yahui Zhang, and Alfred Zong. Cheng Peng acknowledges Gregory M. Stewart for the assistance in drawing FIG. 5. Y.Y.P. is grateful for financial support from the Ministry of Science and Technology of China (Grants No. 2021YFA1401903, No. 2024YFA1408702 and No. 2019YFA0308401) and the National Natural Science Foundation of China (Grants No. 12374143 and No. 11974029). Y.W. acknowledges support by the U.S. Department of Energy, Office of Science, Basic Energy Sciences, under Early Career Award No. DE-SC0024524. N.L.W. acknowledges the support by the National Natural Science Foundation of China (Grant No. 12488201). H.J. acknowledges the support by the National Research Foundation grant funded by the Korea government (MSIT) (grant no. 2019R1F1A1060295). The works at Max Planck POSTECH/Korea Research Initiative were supported by the National Research Foundation of Korea funded by the Ministry of Science and ICT, Grant No. 2022M3H4A1A04074153 and 2020M3H4A2084417. C.P. and J.J.T. acknowledge the support of the U.S. Department of Energy, Office of Science, Basic Energy Sciences under Award No. DE-SC0022216. This tr-RSXS experiment was performed at the SSS-RSXS endstation (proposal number: 2021-2nd-SSS-010) of the PAL-XFEL funded by the Korea government (MSIT). The computation for this research used resources of the National Energy Research Scientific Computing Center, a DOE Office of Science User Facility supported by the Office of Science of the U.S. Department of

Energy under Contract No. DE-AC02-05CH11231 using NERSC award BES-ERCAP0031226.

Author contributions

Y.Y.P. conceived and designed the experiments with suggestions from Y.L., H.J.; X.Y.J., Q.Z.Q., X.Q.C., Q.Z.L., H.J., S.Y.P., M.K., H.D.K and Y.Y.P. performed the tr-RSXS experiment at the PAL-XFEL with the help of B.L. W.J.C., X.H.J. and X.Y.J. synthesized, grew and characterized the $\text{Na}_2\text{Co}_2\text{TeO}_6$ single crystals. L.Y., T.D. and N.L.W. carried out the optical transmission experiment and analyzed the data. Y.Y.P., X.Y.J. and Q.Z.Q. analyzed the tr-RSXS experimental data; C.P. conducted DMRG calculations with guidance and support from Y.W.; Y.Y.P., X.Y.J., J.J.T., C.P. and Y.W. wrote the manuscript with input and discussion from all co-authors.

Competing interests

The authors declare no competing interests.

Additional information

Supplementary information The online version contains supplementary material available at <https://doi.org/10.1038/s41535-025-00737-8>.

Correspondence and requests for materials should be addressed to Yao Wang or Yingying Peng.

Reprints and permissions information is available at <http://www.nature.com/reprints>

Publisher's note Springer Nature remains neutral with regard to jurisdictional claims in published maps and institutional affiliations.

Open Access This article is licensed under a Creative Commons Attribution-NonCommercial-NoDerivatives 4.0 International License, which permits any non-commercial use, sharing, distribution and reproduction in any medium or format, as long as you give appropriate credit to the original author(s) and the source, provide a link to the Creative Commons licence, and indicate if you modified the licensed material. You do not have permission under this licence to share adapted material derived from this article or parts of it. The images or other third party material in this article are included in the article's Creative Commons licence, unless indicated otherwise in a credit line to the material. If material is not included in the article's Creative Commons licence and your intended use is not permitted by statutory regulation or exceeds the permitted use, you will need to obtain permission directly from the copyright holder. To view a copy of this licence, visit <http://creativecommons.org/licenses/by-nc-nd/4.0/>.

© The Author(s) 2025